LETTER

doi:10.1038/nature09417

Melting above the anhydrous solidus controls the location of volcanic arcs

Philip C. England[1] & Richard F. Katz[1]

Segregation of magma from the mantle in subduction zones is one of the principal mechanisms for chemical differentiation of the Earth. Fundamental aspects of this system, in particular the processes by which melt forms and travels to the Earth's surface, remain obscure. Systematics in the location of volcanic arcs, the surface expression of this melting, are widely considered to be a clue to processes taking place at depth, but many mutually incompatible interpretations of this clue exist (for example, see refs 1–6). We discriminate between those interpretations by the use of a simple scaling argument derived from a realistic mathematical model of heat transfer in subduction zones. The locations of the arcs cannot be explained by the release of fluids in reactions taking place near the top of the slab. Instead, the sharpness of the volcanic fronts, together with the systematics of their locations, requires that arcs must be located above the place where the boundary defined by the anhydrous solidus makes its closest approach to the trench. We show that heat carried by magma rising from this region is sufficient to modify the thermal structure of the wedge and determine the pathway through which both wet and dry melts reach the surface.

Volcanic arcs are characterized by sharp fronts whose locations may be described, with misfits of no more than a few kilometres, by small circles on the Earth's surface (Fig. 1 and refs 7 and 8); furthermore, the depth of the top of the slab beneath these fronts falls in a narrow range (~120 ± 40 km; refs 1, 3 and 5). The sharpness of the volcanic fronts implies that a key process in the generation or transport of magma is similarly focused beneath the arcs, but there is no consensus as to what that process may be. A wide range of metamorphic and melting reactions, either in the slab or in the mantle wedge, have been proposed as candidate processes. Some authors suggest that the arcs lie above places where the degree of melting in the mantle wedge becomes high enough for the melt to segregate from the solid[2,4]. Others suggest that the locations of arcs are determined by the release of fluid near the top of the slab in reactions that are either strongly pressure-dependent[1,3,5] or strongly temperature-dependent[6,9]. None of these suggestions has, however, produced a successful quantitative prediction of the location of volcanic arcs. Here we take a different approach: starting with the observed correlation between the descent speed of the slab and its depth beneath the volcanic arcs[8], we use a simple mathematical model to fit the data and reveal the petrological processes responsible for the locations of the arcs.

Although calculations of the full temperature field in subduction zones require numerical models[10], their results can be encapsulated in simple scaling relations that show[11] that temperatures within the mantle wedge and at the top of the slab depend upon a single parameter, $Vr\delta^2/\kappa$. Here V is the convergence rate across the plate boundary, δ is the dip of the slab, r is the radial distance from the wedge corner (Fig. 1), and κ is

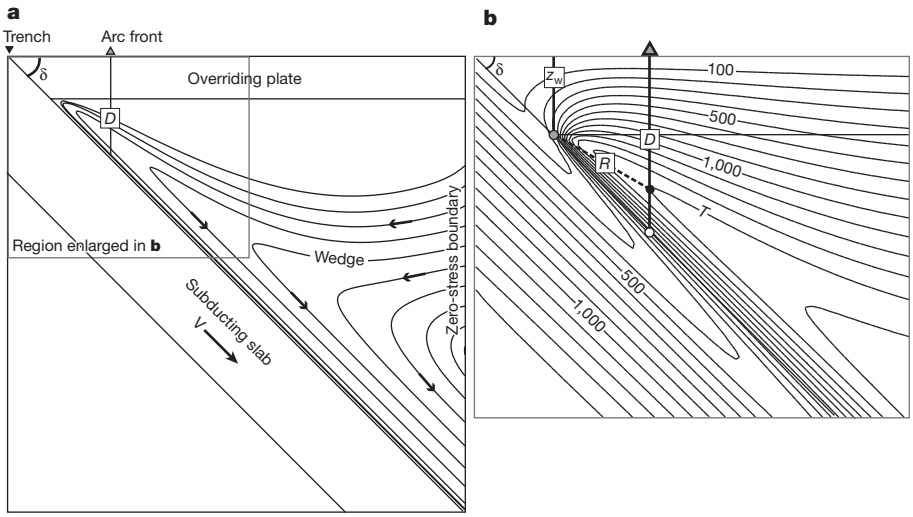

Figure 1 | Idealized cross-sections of a subduction zone, drawn perpendicular to the trench and the island arc. a, Two plates converge at a speed V, with the slab of oceanic lithosphere being subducted at an angle δ beneath the overriding plate. The arc front is a zone a few kilometres wide, across which volcanic activity begins as one moves away from the trench; it lies at a distance D above the top of the slab. The relative motion between slab and overriding plate generates a creeping flow in the wedge of mantle between them, which follows stream lines, shown as curved lines. The corner of the wedge is at a depth z_w. **b**, Enlargement of temperature structure of the rectangle in **a**: Isotherms are shown at intervals of 100 °C. A schematic isotherm, labelled T, has its closest approach to the wedge corner (its 'nose') immediately beneath the volcanic front, at a distance R from the corner (black circle). An open circle marks the top of the slab directly below the corner of this isotherm, at a depth D below the surface. The distance R cannot be determined by observation, but is similar to $R_D = (D - z_w)/\sin\delta$, the radial distance of the top of the slab (open circle) from the wedge corner.

[1]Department of Earth Sciences, South Parks Road, Oxford, OX1 3AN, UK.

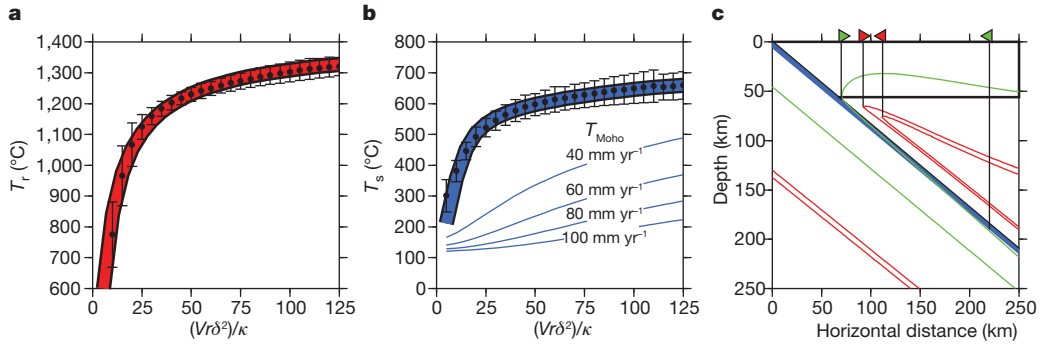

Figure 2 | Scaling relations for temperatures in the core of the mantle wedge, and at the top of the slab. **a**, Maximum temperature in the wedge, T_r, as a function of dimensionless distance from the wedge corner, $Vr\delta^2/\kappa$, where V is convergence speed, δ is dip of the slab, and κ is thermal diffusivity. Dots with error bars indicate the averages and standard deviations of T_r, determined from calculations in which V varies from 10 mm yr^{-1} to 100 mm yr^{-1}, in steps of 10 mm yr^{-1}, while δ varies from 20° to 70° in steps of 10°. The red line corresponds to the theoretical expression for T_r (equation (1)), with $T_0 = 1{,}420$ °C, $B = 3.3$ and $\beta = -0.8$. **b**, As for **a**, but for temperatures within the slab. The thick blue line corresponds to the theoretical expression for T_s, the temperature on the top of the slab (equation (2)), with $C = 1.4$ and $\gamma = -0.06$. Thin blue lines indicate the temperatures at the base of the crust (7 km below the top of the slab) for convergence rates V of 40–100 mm yr^{-1} and a slab dip of 40°. **c**, The temperature structure near the wedge corner for a calculation with a convergence speed V of 80 mm yr^{-1} and a slab dip of 40°. The location of the 500 °C isotherm is shown by green lines and the 1,225 °C and 1,275 °C isotherms are shown by red lines. Green arrowheads show the horizontal extent over which some part of the oceanic crust is at a temperature of 500 °C. Red arrowheads show the range over which the maximum temperature in the mantle wedge lies between 1,225 °C and 1,275 °C (a typical range of temperature represented by the error bars in Fig. 3b). Uncertainties in the temperatures arising from idealizations in the model are discussed in section B2 of the Supplementary Information.

the thermal diffusivity of the mantle. In this scaling, the maximum temperature in the mantle wedge T_r is given by:

$$T_r \approx T_0 \exp\left[-B\left(\frac{Vr\delta^2}{\kappa}\right)^{\beta}\right] \quad (1)$$

while the temperature T_s at the top of the slab is:

$$T_s \approx \frac{T_r}{1 + C\left(Vr\delta^2/\kappa\right)^{\gamma}} \quad (2)$$

where T_0 is a scale temperature, and B, C, β and γ are constants, the values of which depend on the details of the flow near the top of the slab. This scaling was initially derived for a model of subduction zones that treated the mantle as a constant-viscosity fluid[11]; we show here that these relations also hold for the case in which the viscosity has a dependence on temperature that is appropriate for the upper mantle (Fig. 2 and Supplementary Information).

Precise earthquake hypocentral locations[12] reveal that the depth D to the top of the slab beneath the fronts of volcanic arcs is constant, to within a few kilometres, along individual segments of arc, but varies from 80 km to 160 km between different segments[8,13] (Fig. 3). This variation rules out the hypothesis that the arcs are located above the place where the top of the slab reaches a critical pressure corresponding to a single dehydration reaction[1,3,5]. We may also rule out the hypothesis that the release of fluids by temperature-dependent reactions near the top of the slab determines the location of arcs (see, for example, ref. 6). The top of the slab lies within a thermal boundary layer a few tens of kilometres thick, across which there is a temperature difference of ~1,000 °C. Because isotherms within this boundary layer are almost parallel to the slab, any given temperature will be found over a large range of pressure (Fig. 2b, c). Therefore, temperature-dependent processes taking place near the top of the slab cannot be sharply localized, but must occur over a broad range of down-dip distances[14].

In contrast, the steep lateral thermal gradients in the core of the mantle wedge provide a setting in which localization of temperature-dependent processes is likely[2,4]. The maximum temperature in the mantle wedge depends on the dimensionless distance from the wedge corner $Vr\delta^2/\kappa$ (equation (1) and Fig. 2a). Accordingly, we should expect that if a temperature-dependent process is localized beneath the arc, the relevant isotherm will reach its closest approach to the wedge corner (which we refer to below as its 'nose') at a distance R that is inversely proportional to $V\delta^2$. Although R cannot be measured

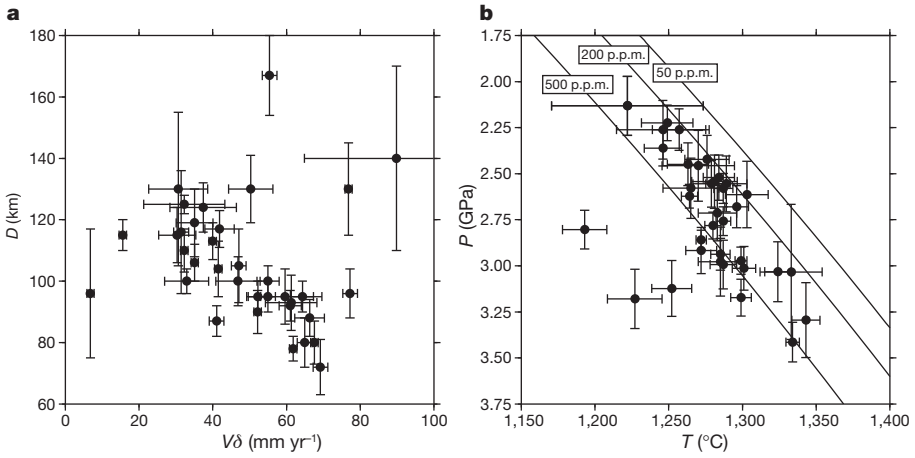

Figure 3 | Systematic variation in depth to the slab beneath volcanic arcs, and its relation to pressure–temperature conditions beneath the arcs. **a**, Depth to the top of the slab beneath volcanic arcs (see Supplementary Information), plotted against $V\delta$ (equation (3)). **b**, Conditions beneath the volcanic fronts estimated from calculations with descent speed, V, and dip, δ, corresponding to the arcs investigated in this paper. Dots show the maximum temperature in the mantle wedge beneath the front, and the pressure at which that temperature is reached. For each calculation, the arc front is taken to lie immediately above the place where the top of the slab reaches the depth D; error bars represent the range in maximum temperature (and the pressure at which it is reached) associated with a ±5 km uncertainty in the horizontal location of the arc front. Lines labelled 50 p.p.m., 200 p.p.m. and 500 p.p.m. correspond to the solidi for peridotite containing these fractions of water[15].

directly, it is very similar to the radial distance $R_D = (D - z_w)/\sin(\delta)$ of the top of the slab from the wedge corner at that location (Fig. 1), thus:

$$\frac{VR_D\delta^2}{\kappa} \approx \frac{V\delta^2(D-z_w)}{\kappa \sin(\delta)} \approx \frac{V\delta(D-z_w)}{\kappa} \quad (3)$$

Here, z_w is the depth to the wedge corner, and we have made the small-angle approximation $\sin(\delta) \approx \delta$. Hence, for z_w constant or varying little in comparison with D, we should expect D to vary inversely with $V\delta$.

We can make a reliable determination of D for 35 arcs (Supplementary Information); the Spearman rank-order correlation coefficient between D and $V\delta$ for these arcs (Fig. 3b) is -0.34, which is significant at the 95% level of confidence. The significance of the correlation is sensitive to the presence of five arcs with large uncertainties in D (identified in the discussion of Supplementary Fig. 1); the confidence level for the correlation exhibited when these five arcs are excluded is above 99%. Thirty arc segments, with a total length of 22,000 km, exhibit the relationship between D and $V\delta$ that is predicted by equation (3), whereas five arc segments with a total length of ~4,000 km do not lie on the trend. (See Supplementary Material for further discussion.) We therefore conclude that the global systematics[8,13] strongly support the hypothesis that the locations of volcanic arcs are determined by a temperature-dependent process taking place in the wedge[2,4].

To estimate the conditions under which this process takes place, we carried out calculations of steady-state wedge thermal structure for combinations of slab dip and convergence rate corresponding to the 35 individual arcs in Fig. 3a. The maximum temperature in the column of mantle beneath the location of the arc, and the pressure at which that temperature is reached, form an array between about 1,250 °C and 1,325 °C, and 2–3.5 GPa (Fig. 3b) that corresponds closely to the range of pressure–temperature conditions for the melting of peridotite in the presence of between 200 p.p.m. H_2O and 500 p.p.m. H_2O (ref. 15). These water contents are about ten times lower than the concentrations estimated for wet melting beneath arcs, but are representative of the water contents of the mantle beneath backarc basins[16]. In what follows, we refer to such H_2O concentrations as "anhydrous" to distinguish them from the hydrous melts that are much more abundant in the wedge.

It is generally accepted that hydrous melting pervades the mantle wedge, but it has been suggested that the arc front is located somewhere above the region in which the temperature in the wedge exceeds the anhydrous solidus, because the degree of hydrous melting increases rapidly there[2,4]. Melt may also be produced in this temperature range as a result of anhydrous decompression melting of upwelling mantle; indeed, the existence of distinct regimes of melting beneath the arcs has been inferred from the eruption of low-water-content, tholeiitic melt from arc volcanoes that also erupt typical hydrous melts[17–21]. Geodynamic models show, however, that either type of melting occupies a broad region of the wedge core, extending from beneath the arc front towards the back-arc[22,23]. Any explanation for the localization of the arc fronts that invokes melts produced over this broad volume must therefore include a mechanism for focusing the melts to the line beneath the arcs.

The interaction of rising magma with the thermal boundary layer at the top of the wedge provides this mechanism. As the rising magma hits this boundary, it begins to crystallize, forming an impermeable barrier above a sloping, high-porosity channel[23,24]. Such interaction requires sufficient crystallization to seal the pore space against vertical magmatic flow[25]; this condition is met at temperatures above the anhydrous solidus, where isobaric productivity is high and small decreases in temperature result in significant crystallization, but not below it, where isobaric productivity is low[15,26]. We therefore propose, as sketched in Fig. 4a, that the high-porosity channel terminates at the 'nose' of the anhydrous solidus. This 'nose' is controlled by temperature, so its location will depend upon $V\delta$, consistent with the observations (Fig. 3).

If the advective flux of heat carried by the magma is of the same order as the vertical conductive heat flux, the melt arriving at the nose of the solidus will erode the cold boundary layer at the top of the wedge and bow upward the solidi for both wet and dry melting. The rate of heat transfer by the melt is $\sim ML$, where M is the mass flow of magma and L is its latent heat per unit mass. The conductive heat flux is $\sim k\Delta T/h$, where k is thermal conductivity, ΔT is the temperature difference between the solidus and the surface temperature, and h is the depth to the 'nose' of the solidus beneath the arc. This argument, expanded in the Supplementary Information, shows that the ratio of these two quantities controls the efficiency of thermal erosion:

$$\mathcal{M} = \frac{MLh}{k\Delta T} \quad (4)$$

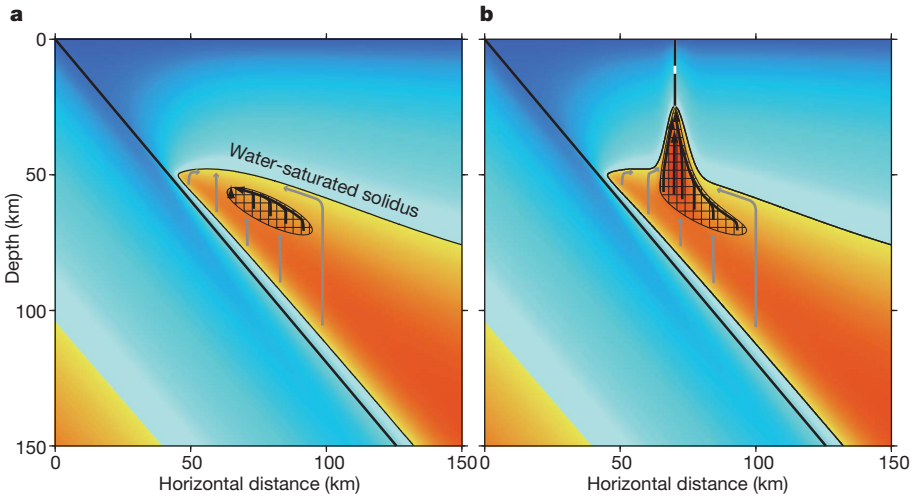

Figure 4 | A sketch of the process that determines the position of volcanoes. The top of the slab is indicated by the diagonal line starting at the origin. The black line separating the blue and yellow-to-red colours within the wedge represents the water-saturated solidus of the mantle, the cross-hatched region is above the nominally anhydrous solidus of ambient mantle. **a**, The distribution of temperature and melting without heat transport by migrating melt. Grey and black arrows show melt formed above the water-saturated and anhydrous solidi, respectively, rising, then travelling through high-porosity channels to the 'noses' of the solidi. **b**, A schematic depiction of how melt transport, indicated by arrows, would modify the distribution in **a**. Magma rising from the 'nose' of the dry solidus heats the region immediately above, deflecting upwards the dry and wet solidi so that they both reach their shallowest depth in the same horizontal location. Each type of melt travels laterally and upward along its respective solidus towards this location. Melts eventually penetrate the lithosphere by hydrofracture and dyking. In the case of low permeability in the wedge, advection of melt by the moving mantle can cause the trajectories to deviate horizontally[23]: this process could affect the details of the sketch.

For reasonable estimates of the rate of mass flux into arc volcanoes[22,27–30] $\mathcal{M} \approx 0.8$, which is sufficient to perturb upward the location of the anhydrous solidus by >40% of its depth (Supplementary Fig. 4). In consequence, all melt migrates towards the place where the solidus is bowed upward—including melt generated closer to the trench (Fig. 4b).

In summary, the observed systematics in the location of the volcanic arcs shows that the mechanisms whereby the melt reaches the Earth's surface are controlled by the dynamics of the wedge, not by any locally concentrated release of fluid in reactions taking place near the top of the slab. In our model, magma formed at temperatures above the anhydrous solidus in the wedge is focused trench-ward, to the 'nose' of the region bounded by that solidus. Above the 'nose', thermal erosion by rising magma establishes the pathway that all melts, hydrous or anhydrous, take to reach the arc volcanoes. Future analysis, including calculations that incorporate the physics of melt migration[31], will help to clarify this hypothesis.

METHODS SUMMARY

Calculations of thermal structure of subduction zones. Our calculation of the thermal structure of subduction zones employs a finite-volume discretization of the incompressible, variable-viscosity Stokes equation and steady-state, advection-diffusion energy equation on a uniformly spaced, staggered Cartesian mesh. It uses a Newton–Krylov solver provided by the Portable, Extensible Toolkit for Scientific Computation (http://www.mcs.anl.gov/petsc). The code has been benchmarked against other numerical solutions for this type of problem. The viscosity η is given by an Arrhenius law for diffusion creep of olivine:

$$\eta = A \exp\left(\frac{E + PV^*}{RT}\right) \quad (5)$$

with activation energy E and activation volume V^* of 375 kJ mol^{-1} and 5×10^{-6} m^3 mol^{-1}, respectively, and pre-exponential $A = 1.8 \times 10^7$ Pa s.

The domain is 600 km by 600 km, oriented as shown in Fig. 1, with a mesh spacing of 1 km. We have checked convergence of our solutions by comparing them, for combinations of parameters that span the range of interest, against solutions with mesh spacing of 0.5 km. We find differences between the two meshes at the level of less than 10 °C between temperatures calculated on the top of the slab or near the wedge corner.

Measurement of depth to top of slab beneath arcs. We apply the methods of ref. 8 to the 45 arc segments studied by ref. 13. For each arc segment we formed cross-sections of the seismicity and estimated D as described by ref. 8. We used the tables given in the supplementary information of ref. 13 to check whether the segment boundaries of the two studies agreed; except where noted in our Supplementary Table, the disagreements were minor and we used the segment boundaries of ref. 8.

Full Methods and any associated references are available in the online version of the paper at www.nature.com/nature.

Received 2 February; accepted 23 July 2010.

1. Gill, J. *Orogenic Andesites and Plate Tectonics* (Springer, 1981).
2. Kushiro, I. in *Magmatic Processes: Physicochemical Principles* (ed. Mysen, B.) Vol. 1, 165–181 (Geochemical Society Special Publication, 1987).
3. Tatsumi, Y. & Eggins, S. *Subduction Zone Magmatism* (Blackwell Science, 1995).
4. Schmidt, M. & Poli, S. Experimentally based water budgets for dehydrating slabs and consequences for arc magma generation. *Earth Planet. Sci. Lett.* **163,** 361–379 (1998).
5. Tatsumi, Y. The subduction factory: how it operates in the evolving Earth. *GSA Today* **15,** 4–10 (2005).
6. Grove, T. L., Till, C. B., Lev, E., Chatterjee, N. & Médard, E. Kinematic variables and water transport control the formation and location of arc volcanoes. *Nature* **459,** 694–697 (2009).
7. Tovish, A. & Schubert, G. Island arc curvature, velocity of convergence and angle of subduction. *Geophys. Res. Lett.* **5,** 329–332 (1978).
8. England, P. C., Engdahl, E. R. & Thatcher, W. Systematic variation in the depths of slabs beneath arc volcanoes. *Geophys. J. Int.* **156,** 377–408 (2004).
9. Ulmer, P. & Trommsdorff, V. Serpentine stability to mantle depths and subduction-related magmatism. *Science* **268,** 858–861 (1995).
10. van Keken, P. *et al.* A community benchmark for subduction zone modeling. *Phys. Earth Planet. Inter.* **171,** 187–197 (2008).
11. England, P. & Wilkins, C. A simple analytical approximation to the temperature structure in subduction zones. *Geophys. J. Int.* **159,** 1138–1154 (2004).
12. Engdahl, E., van der Hilst, R. & Buland, R. Global teleseismic earthquake relocation with improved travel times and procedures for depth determination. *Bull. Seismol. Soc. Am.* **88,** 722–743 (1998).
13. Syracuse, E. M. & Abers, G. A. Global compilation of variations in slab depth beneath arc volcanoes and implications. *Geochem. Geophys. Geosyst.* **7** (5), Q05017, doi: 10.1029/2005GC001045 (2006).
14. England, P. C. & Katz, R. F. Global systematics of arc volcano position. *Nature* doi: 10.1038/nature09154 (in the press).
15. Katz, R., Spiegelman, M. & Langmuir, C. A new parameterization of hydrous mantle melting. *Geochem. Geophys. Geosyst.* **4** (9), 1073, doi: 10.1029/2002GC000433 (2003).
16. Kelley, K. A. *et al.* Mantle melting as a function of water content beneath back-arc basins. *J. Geophys. Res.* **111,** B09208, doi: 10.1029/2005JB003732 (2006).
17. Baker, M., Grove, T. & Price, R. Primitive basalts and andesites from the Mt. Shasta region, N. California—products of varying melt fraction and water content. *Contrib. Mineral. Petrol.* **118,** 111–129 (1994).
18. Sisson, T. & Bronto, S. Evidence for pressure-release melting beneath magmatic arcs from basalt at Galunggung, Indonesia. *Nature* **391,** 883–886 (1998).
19. Elkins-Tanton, L., Grove, T. & Donnelly-Nolan, J. Hot, shallow mantle melting under the Cascades volcanic arc. *Geology* **29,** 631–634 (2001).
20. Cameron, B. *et al.* Flux versus decompression melting at stratovolcanoes in southeastern Guatemala. *J. Volcanol. Geotherm. Res.* **119,** 21–50 (2003).
21. Tatsumi, Y. & Suzuki, T. Tholeiitic *vs* calc-alkalic differentiation and evolution of arc crust: constraints from melting experiments on a basalt from the Izu-Bonin-Mariana arc. *J. Petrol.* **50,** 1575–1603 (2009).
22. Conder, J., Wiens, D. & Morris, J. On the decompression melting structure at volcanic arcs and back-arc spreading centers. *Geophys. Res. Lett.* **29,** 1727, doi: 10.1029/2002GL015390 (2002).
23. Cagnioncle, A.-M., Parmentier, E. M. & Elkins-Tanton, L. T. Effect of solid flow above a subducting slab on water distribution and melting at convergent plate boundaries. *J. Geophys. Res.* **112,** B09402, doi: 10.1029/2007JB004934 (2007).
24. Sparks, D. & Parmentier, E. Melt extraction from the mantle beneath spreading centers. *Earth Planet. Sci. Lett.* **105,** 368–377 (1991).
25. Spiegelman, M. Physics of melt extraction: theory, implications, and applications. *Phil. Trans. R. Soc. Lond. A* **342,** 23–41 (1993).
26. Hirschmann, M. M., Asimow, P. D., Ghiorso, M. S. & Stolper, E. M. Calculation of peridotite partial melting from thermodynamic models of minerals and melts. III. Controls on isobaric melt production and the effect of water on melt production. *J. Petrol.* **40,** 831–851 (1999).
27. Crisp, J. Rates of magma emplacement and volcanic output. *J. Volcanol. Geotherm. Res.* **20,** 177–211 (1984).
28. Reymer, A. & Schubert, G. Phanerozoic addition rates to the continental crust and crustal growth. *Tectonics* **3,** 63–77 (1984).
29. Dimalanta, C., Taira, A., Yumul, G., Tokuyama, H. & Mochizuki, K. New rates of western Pacific island arc magmatism from seismic and gravity data. *Earth Planet. Sci. Lett.* **202,** 105–115 (2002).
30. White, S., Crisp, J. & Spera, F. Long-term volumetric eruption rates and magma budgets. *Geochem. Geophys. Geosyst.* **7,** Q03010 (2006).
31. Katz, R. Magma dynamics with the enthalpy method: benchmark solutions and magmatic focusing at mid-ocean ridges. *J. Petrol.* **49,** doi: 10.1093/petrology/egn058 (2008).

Supplementary Information is linked to the online version of the paper at www.nature.com/nature.

Acknowledgements We are grateful to T. Grove and E. Lev for their free exchange of ideas and data concerning their paper (ref. 6), and to C. Langmuir for comments that helped us to improve the manuscript. We thank E. Syracuse for providing hypocentral locations. Numerical models were run on computational clusters at the Oxford Supercomputing Centre.

Author Contributions R.F.K. wrote the code for the numerical experiments; P.C.E. carried out the re-analysis of depth-to-slab (Fig. 3 and Supplementary Information). Both authors participated equally in developing the ideas presented in this paper and in writing it.

Author Information Reprints and permissions information is available at www.nature.com/reprints. The authors declare no competing financial interests. Readers are welcome to comment on the online version of this article at www.nature.com/nature. Correspondence and requests for materials should be addressed to P.C.E. (philip@earth.ox.ac.uk).

METHODS

Calculations of thermal structure of subduction zones. Our calculation of the thermal structure of subduction zones employs a finite-volume discretization of the incompressible, variable-viscosity Stokes equation and steady-state, advection-diffusion energy equation on a uniformly spaced, staggered Cartesian mesh[32]. It uses a Newton–Krylov solver provided by the Portable, Extensible Toolkit for Scientific Computation[33,34]. The code has been benchmarked against other numerical solutions for this type of problem[10]. The viscosity η is given by an Arrhenius law for diffusion creep of olivine:

$$\eta = A \exp\left(\frac{E + PV^*}{RT}\right) \quad (6)$$

with activation energy E and activation volume V^* of 375 kJ mol^{-1} and 5×10^{-6} m^3 mol^{-1}, respectively, and pre-exponential $A = 1.8 \times 10^7$ Pa s (refs 35 and 36).

The domain is composed of three subdomains, the slab, the wedge, and the overlying lid. Velocity in the slab subdomain is prescribed using the convergence rate and the slab dip; velocity in the lid is forced to equal zero. Within the wedge we solve the incompressible Stokes equation with no buoyancy term. There are no-slip conditions on the wedge–lid and wedge–slab boundaries, and there is a no-stress condition applied at the wedge inflow–outflow boundary. Temperature is fixed at zero on the top of the domain; the slab is given a temperature profile using the one-dimensional conducting slab solution; this solution is also applied to fix the temperatures on the inflow boundary. Complete details are provided in ref. 10.

The domain is 600 km by 600 km, oriented as shown in Fig. 1, with a mesh spacing of 1 km. We have checked convergence of our solutions by comparing them, for combinations of parameters that span the range of interest, against solutions with mesh spacing of 0.5 km. We find differences between the two meshes at the level of less than 10 °C between temperatures calculated on the top of the slab or near the wedge corner.

An important parameter in thermal models of subduction zones is the depth at which the slab couples to the mantle wedge with a no-slip condition[37]. The maximum extent of shallowly dipping thrust faulting on the plate interface in subduction zones is about 45 km (ref. 38) and, allowing for a transitional zone of aseismic sliding below this depth, we fix the depth to the top of full coupling between wedge and slab at 56 km.

Measurement of depth to top of slab beneath arcs. We apply the methods of ref. 8 to the 45 arc segments studied by ref. 13. For each arc segment we formed cross-sections of the seismicity and estimated D as described by ref. 8. We used the tables given in the supplementary information of ref. 13 to check whether the segment boundaries of the two studies agreed; except where noted in our Supplementary Table, the disagreements were minor and we used the segment boundaries of ref. 8.

We could not obtain reliable estimates of D for seven arcs, either because of the sparsity of earthquakes or because the volcanoes are spread out so widely that a clear volcanic front cannot be identified (see remarks on individual arcs, in the Supplementary Information). We combined the remaining volcanoes into 35 arc segments for which D estimated by the two different methods can be reconciled. An example of illustrating the two approaches, and their reconciliation in one of the more problematic arcs, can be seen in Supplementary Fig. 2. The Marianas, Lesser Antilles, and Vanuatu arcs are treated as single arcs here; each is split into northern and southern segments by ref. 41.

32. Knepley, M., Katz, R. & Smith, B. in *Numerical Solution of Partial Differential Equations on Parallel Computers* Vol. 51 *Lecture Notes in Computational Science and Engineering* (eds Bruaset, A. & Tveito, A.) 413–438 (Springer, 2006).
33. Balay, S. *et al. Portable, Extensible Toolkit for Scientific Computation (PETSc)*; ⟨http://www.mcs.anl.gov/petsc⟩ (2001).
34. Katz, R., Knepley, M., Smith, B., Spiegelman, M. & Coon, E. Numerical simulation of geodynamic processes with the Portable Extensible Toolkit for Scientific Computation. *Phys. Earth Planet. Inter.* **163,** 52–68 (2007).
35. Karato, S. & Wu, P. Rheology of the upper mantle—a synthesis. *Science* **260,** 771–778 (1993).
36. Hirth, G. & Kohlstedt, D. in *Inside the Subduction Factory* (ed. Eiler, J.) Vol. 138, 83–105 (AGU Geophysical Monograph, American Geophysical Union, 2003).
37. Conder, J. A case for hot slab surface temperatures in numerical viscous flow models of subduction zones with an improved fault zone parameterization. *Phys. Earth Planet. Inter.* **149,** 155–164 (2005).
38. Tichelaar, B. W. & Ruff, L. Depth of seismic coupling along subduction zones. *J. Geophys. Res.* **98,** 2107–2037 (1993).